Single-Atom Catalysis Hot Paper

How to cite: *Angew. Chem. Int. Ed.* **2023**, *62*, e202218460
International Edition: doi.org/10.1002/anie.202218460
German Edition: doi.org/10.1002/ange.202218460

Engineering a Copper Single-Atom Electron Bridge to Achieve Efficient Photocatalytic CO_2 Conversion

Gang Wang[+], Yan Wu[+], Zhujie Li[+], Zaizhu Lou, Qingqing Chen, Yifan Li, Dingsheng Wang, and Junjie Mao**

Abstract: Developing highly efficient and stable photocatalysts for the CO_2 reduction reaction (CO_2RR) remains a great challenge. We designed a Z-Scheme photocatalyst with N–Cu_1–S single-atom electron bridge (denoted as Cu-SAEB), which was used to mediate the CO_2RR. The production of CO and O_2 over Cu-SAEB is as high as 236.0 and 120.1 $\mu mol\, g^{-1}\, h^{-1}$ in the absence of sacrificial agents, respectively, outperforming most previously reported photocatalysts. Notably, the as-designed Cu-SAEB is highly stable throughout 30 reaction cycles, totaling 300 h, owing to the strengthened contact interface of Cu-SAEB, and mediated by the N–Cu_1–S atomic structure. Experimental and theoretical calculations indicated that the SAEB greatly promoted the Z-scheme interfacial charge-transport process, thus leading to great enhancement of the photocatalytic CO_2RR of Cu-SAEB. This work represents a promising platform for the development of highly efficient and stable photocatalysts that have potential in CO_2 conversion applications.

Introduction

Inspired by natural photosynthesis, solar-driven conversion of CO_2 and H_2O into chemical fuels and O_2 is recognized as an attractive and sustainable technique to solve the energy crisis and environmental pollution.[1] Some photocatalysts have already been developed for the photocatalytic reduction of CO_2 with pure water.[1b] Unfortunately, the CO_2 conversion efficiency and stability of these photocatalysts are still far from the threshold required for industrial applications. The fundamental reason is the inefficient migration and utilization of photo-generated charge carriers, which restricts the CO_2 conversion ability of these photocatalysts.[2] Hence, exploring advanced strategies to achieve effective separation and transport of charge carriers in photocatalysts is highly desirable, but it remains a great challenge.

Enormous efforts have been devoted to promoting the separation of photo-generated charge carriers in photocatalysts, including element doping, co-catalyst loading, defect engineering, Z-scheme system construction, and so on.[3] Among them, the Z-scheme charge-transfer mode has proved to be a very promising method to improve the separation efficiency of charge carriers. Notably, the construction of an electron bridge (EB) at the interface is a crucial factor to ensure the separation of photo-generated carriers where there is a relatively strong redox potential across the components of a Z-scheme system.[4] As for the all-solid-state and direct Z-scheme systems, metal nanoparticles and the internal electric field can act as EBs to realize a "Z"-shaped charge-transport pathway under light irradiation.[5] However, these EBs always suffer from unstable contact at the interface and inefficient interfacial charge transport. Either of them can result in decreased photocatalytic performances. It is an urgent task to develop a new strategy to construct an EB capable of rapid charge transfer and stable contact at the interface. Recently, single-atom-site catalysts have emerged, showing great potential in catalysis because of their high atom utilization efficiency and excellent catalytic performances.[6] These beneficial properties can be attributed to the strong metal–support interaction constructed at the atomic level, which improves the stability of the interfacial structure.[7] Moreover, the large number of active sites and flexible coordination environment can modulate their interfacial charge-transfer behaviors.[8] Therefore, designing a single-atom electron bridge (SAEB) may overcome the unstable contact and inefficient interfacial charge transport in Z-scheme photocatalysts. However, to the best of our knowledge, designing SAEBs in Z-scheme systems for efficient, selective, and stable CO_2 reduction with pure water is rarely explored.

Herein, the SAEB of a N–Cu_1–S species is first proposed for fabricating a Cu-SAEB Z-scheme photocatalyst to

[*] Dr. G. Wang,[+] Y. Wu,[+] Q. Chen, Y. Li, Prof. J. Mao
Key Laboratory of Functional Molecular Solids, Ministry of Education, College of Chemistry and Materials Science, Anhui Normal University
Wuhu, 241002 (P. R. China)
E-mail: maochem@ahnu.edu.cn
Dr. Z. Li[+]
Advanced Technology Research Institute, Beijing Institute of Technology
Jinan, 250300 (P. R. China)
Prof. Z. Lou
Guangdong Provincial Key Laboratory of Nanophotonic Manipulation, Institute of Nanophotonics, Jinan University
Guangzhou, 511443 (P. R. China)
Prof. D. Wang
Department of Chemistry, Tsinghua University
Beijing, 100084 (P. R. China)
E-mail: wangdingsheng@mail.tsinghua.edu.cn
[+] These authors contributed equally to this work

achieve highly active and stable CO_2RR performance. Cu-SAEB demonstrated excellent photocatalytic CO_2RR activity in the absence of sacrificial agents, with CO and O_2 formation rates of 236.0 and 120.1 $\mu mol\,g^{-1}\,h^{-1}$, respectively, which were much higher than those of Cu-NPEB (the sample with Cu nanoparticles as the EB) and other corresponding control samples. These performances almost represent one of the best photocatalysts for converting CO_2 and H_2O to CO and stoichiometric amounts of O_2. Furthermore, the dynamics of charge carriers and theoretical calculations confirmed that the N–Cu_1–S species could serve as a SAEB to achieve a Z-scheme charge-transfer mode to greatly accelerate the recombination of photogenerated electrons and holes with a relatively lower redox potential. Accordingly, the lifetimes of carriers with a strong redox potential can be greatly prolonged during light irradiation, which resulted in an enhanced CO_2RR performance for Cu-SAEB. Benefiting from the formation of SAEBs at the Z-scheme interface, the Cu-SAEB photocatalyst proved to be extremely stable throughout at least 30 cycles ($\geq$300 h).

Results and Discussion

Cu-SAEB was obtained via a two-step method (details are shown in the Supporting Information). First, MoS_2 (MS) was decorated with Cu species to obtain Cu_1/MS (the Cu content is about 1.2 wt%) using a photo-reduction method. Thereafter, a 15 wt% mass ratio of Cu_1/MS was coated on the surface of MIL, resulting in Cu-SAEB after a hydrothermal process. The X-ray diffraction (XRD) patterns of Cu-SAEB confirm the co-existence of hexagonal MS and standard MIL (Figures S1 and S2), which was also proved by Fourier-transform infrared spectroscopy (FTIR) and Raman spectroscopy results (Figures S3 and S4). Significant decreases were observed in the specific surface areas of MS/MIL and Cu-SAEB (Figure S5 and Table S1), suggesting that the surface cavities of MIL can be covered by well-dispersed MS or Cu_1/MS nanosheets.

The morphology of Cu-SAEB was characterized by scanning electron microscopy (SEM) and transmission electron microscopy (TEM) (Figures S6 and S7). Figure 1a displays that Cu_1/MS nanosheets are uniformly coated on the surface of MIL, resulting in an encapsulation structure. The aberration-corrected high-angle annular dark-field scanning TEM (AC HAADF-STEM) image presented in Figure 1b, combined with the corresponding energy-dispersive X-ray spectroscopy (EDS) results in Figure 1c, confirm the uniform dispersion of Cu in the Cu-SAEB encapsulation structure. The encapsulation structures of MS/MIL (the sample without additional EB) and Cu-NPEB were similar to that of Cu-SAEB (Figures S8 and S9). No obvious nanosheets can be observed on the surface of MIL (Figure S10) in Cu_1/MS + MIL, the sample where Cu_1/MS and MIL are mechanically mixed, revealing that the encapsulation structure of Cu-SAEB cannot be formed via random mixing. Zeta potentials indicated that the electrostatic interaction might be the binding driving force for the formation of the encapsulation structure (Figure S11). In addition, the morphologies of reference samples, including the different Cu contents loaded on MS, Cu NPs/MS, and MIL, are also shown in Figure S12.

X-ray photoelectron spectroscopy (XPS) measurements were conducted to investigate the chemical information of Cu species in samples. The Cu 2p XPS spectra suggest the co-existence of Cu^+ and Cu^{2+} in Cu-SAEB (Figure S13) and the single valence state of Cu in Cu_1/MS (Figure S14). Furthermore, the accompanying Auger peaks (Cu LMM) at 568.4 and 570.3 eV can be ascribed to the binding energies of Cu–S and Cu–N bonds in Cu-SAEB, respectively (Figure 1d). As for the N 1s and S 2p XPS spectra of Cu-SAEB (Figure 1e,f), the binding energies at 398.8 and 162.6 eV also correspond to the formation of Cu–N and Cu–S bonds, respectively. X-ray absorption fine structure (XAFS) was further determined for Cu-SAEB to ascertain the coordination environment of Cu. As shown in Figure 1g, the near-edge position of Cu-SAEB is between those of CuS and CuPc, which implies that the average oxidation state of Cu species in Cu-SAEB is between these two references. This difference may be attributed to the co-existence of Cu–S and Cu–N coordination modes in Cu-SAEB. Figure 1h displays the Fourier-transform EXAFS (FT-EXAFS) spectra of Cu-SAEB and the references (Cu foil, CuS, and CuPc). It can be observed that the main FT-EXAFS peak of Cu-SAEB is between the scattering of Cu–N and Cu–S coordination. The wavelet transform (WT) maximum of Cu-SAEB (4.3 $Å^{-1}$) is also between those of CuPc (3.8 $Å^{-1}$) and CuS (4.8 $Å^{-1}$) (Figure S15). Summarizing the XAFS and XPS results, the co-existence of Cu–S and Cu–N bonds is confirmed, which is a highly probable form of N–Cu–S coordination in Cu-SAEB. In addition, the least-squares EXAFS fitting method was applied to quantify the local structural parameters of Cu species in Cu-SAEB (Figure 1i and Table S2). The fitting results suggest that the coordination number of Cu species is four, and the average bond lengths of Cu–N and Cu–S are about 1.98 Å and 2.26 Å, respectively. Furthermore, theoretical simulations were carried out to identify the most stable atomic structure in Cu-SAEB. These results suggest that the Cu single atom is coordinated with one N atom and three S atoms (Figure S16) in Cu-SAEB. For comparison, the chemical environments of Cu single atoms in Cu_1/MS and Cu_1/MS + MIL were confirmed, and are similar to the Cu–S coordination in the CuS reference (Figures S17–S19). In addition, the Cu NPs in Cu-NPEB were also proved by XAFS and FT-EXAFS spectra (Figure S19).

The band structures of MS, Cu_1/MS, and MIL were investigated by UV/Vis diffuse reflectance spectroscopies (DRS) and Mott–Schottky measurements. As shown in Figure 2a, the absorption edge of MIL is about 512 nm, while MS and Cu_1/MS have considerable absorption in the full spectrum. The band structures of samples have been calculated via the Tauc and Mott–Schottky plots (Figures S20–S22). As for the composite photocatalysts, the interactions of components significantly affect the direction of electron transfer at their contact interface during light irradiation. XPS was performed to compare the binding

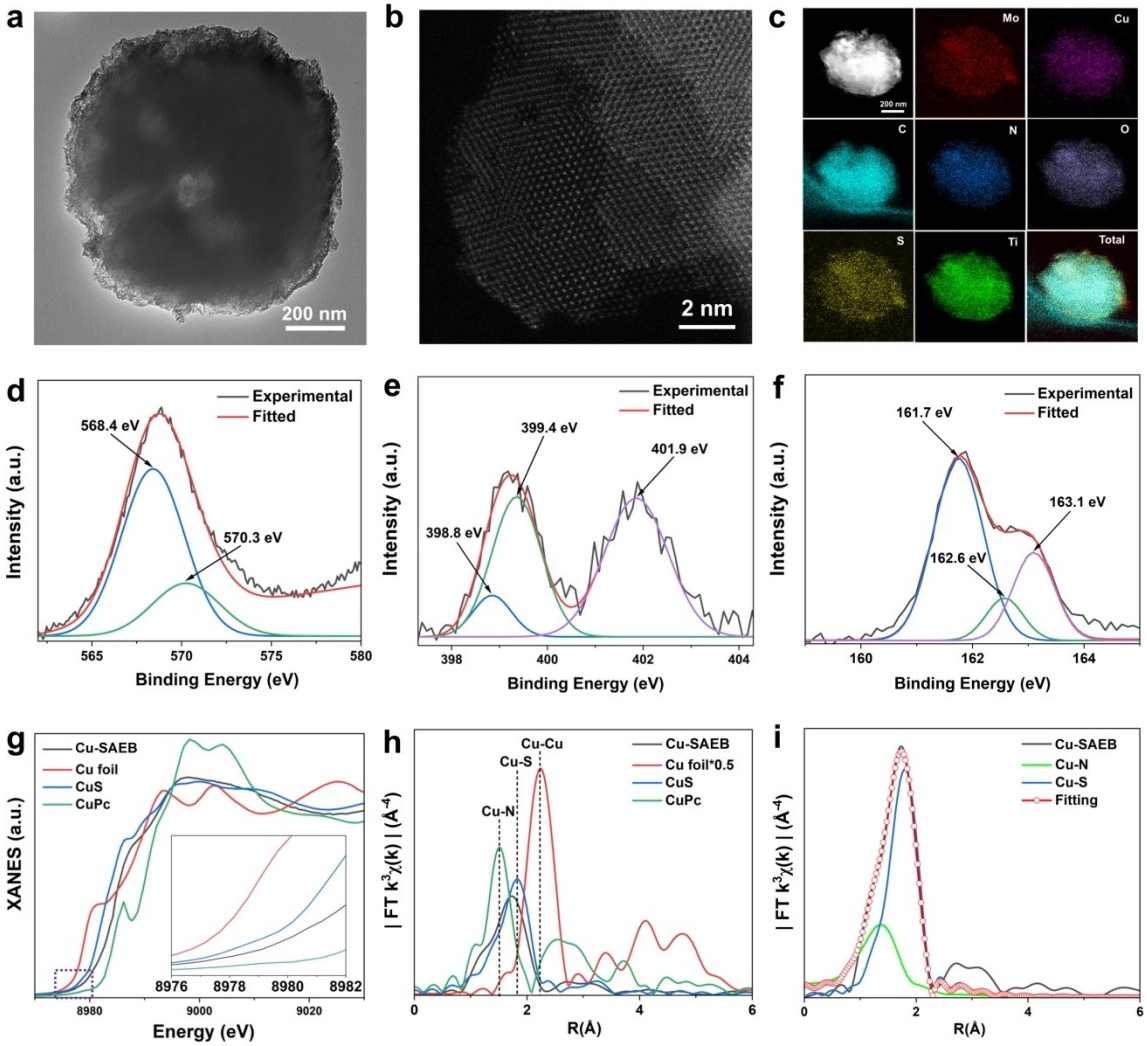

Figure 1. (a) Low-magnification TEM image of Cu-SAEB. (b) Atomic resolution AC HAADF-STEM image of Cu-SAEB. (c) EDS elemental mapping of Cu-SAEB. XPS spectra of (d) Cu LMM, (e) N 1s, and (f) S 2p of Cu-SAEB. (g) Cu K-edge XANES spectra of Cu-SAEB and the reference samples. The inset is the magnified image. (h) FT-EXAFS spectra of Cu-SAEB and the reference samples. (i) FT-EXAFS fitting results of Cu-SAEB.

energies of the components before and after light irradiation, which can strongly validate the charge-transfer direction in composite photocatalysts. First, the samples underwent the same photocatalytic process (details are shown in the Supporting Information) and are referred to as MS/MIL-hν, Cu-NPEB-hν, and Cu-SAEB-hν. As shown in Figure 2b,c, the binding energy of Ti 2p in MS/MIL-hν has a positive shift compared to that of MIL, while Mo 3d shifts to a lower binding energy after light irradiation. These observations suggest that photo-generated electrons can transfer from MIL to MS under light irradiation, indicating the formation of a type-II charge-transfer mode in MS/MIL. However, for Cu-SAEB-hν, the binding energies of Ti 2p and Mo 3d move in the opposite direction compared with those of MS/MIL-hν. This indicates that the electrons transfer from Cu_1/MS to MIL, which confirms the formation of the Z-scheme charge-transfer mode in Cu-SAEB. In other words, N–Cu_1–S can serve as a SAEB to transfer the photo-generated electrons from Cu_1/MS to MIL at the contact interface of Cu-SAEB. As a result, the type-II charge-transfer mode can be transformed to a Z-scheme mode owing to the existence of N–Cu_1–S species in Cu-SAEB. Meanwhile, similar shifts in the binding energies of Ti 2p and Mo 3d have also been detected in Cu-NPEB-hν, implying the formation of Z-scheme charge-transfer behavior in Cu-NPEB. To further investigate whether the charge transfer in our photocatalysts is characteristic of Z-Schemes, $^{\bullet}O_2^-$ radical trapping experiments were carried out using 5, 5-dimethyl-1-pyrroline *N*-oxide (DMPO) as the trapping agent. The conduction band minimum (CBM) potential of MIL is about −0.77 vs. NHE, which is sufficient to trigger the reduction of O_2 into $^{\bullet}O_2^-$ (−0.33 V vs. NHE) (Figure S23a). The CBM potentials of bulk MS, Cu_1/MS, and Cu NPs/MS are not negative enough to reduce O_2 to $^{\bullet}O_2^-$ (Figure S23b-d). Compared with the results of $^{\bullet}O_2^-$ radical trapping experiments for MIL, the intensity of DMPO-$^{\bullet}O_2^-$ peaks for MS/MIL decrease significantly during light irradiation (Figure 2d). This result supports the type-II charge-

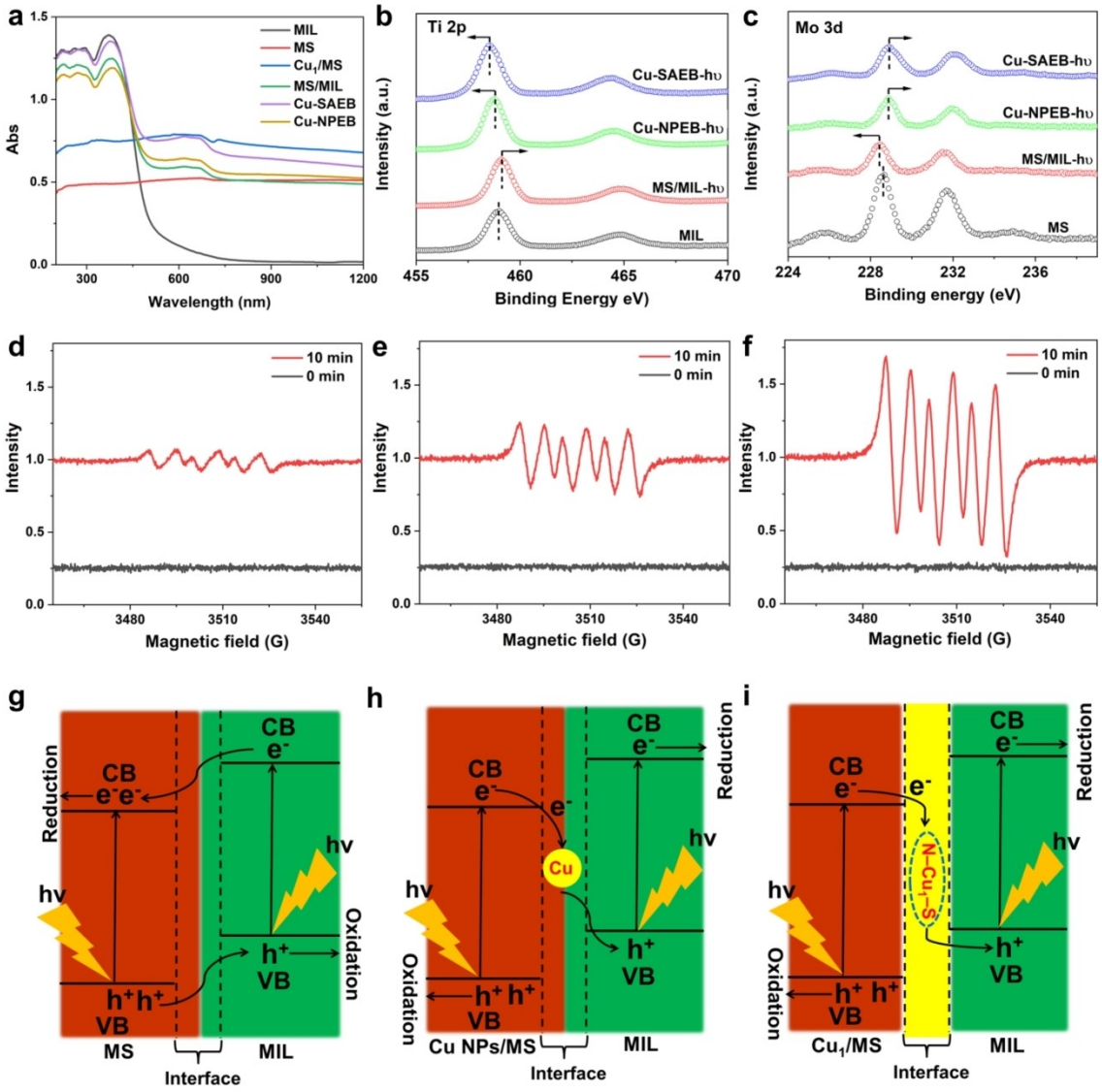

Figure 2. (a) UV/Vis DRS of samples. XPS spectra of (b) Ti 2p and (c) Mo 3d of Cu-SAEB-hv and the corresponding comparison samples. DMPO spin-trapping EPR spectra recorded for $^{\bullet}O_2^-$ under light irradiation upon (d) MS/MIL, (e) Cu-NPEB, and (f) Cu-SAEB. Electron-transfer process models of (g) MS/MIL, (h) Cu-NPEB, and (i) Cu-SAEB.

transport mode (Figure 2g), leading to an insufficient reduction potential of MS/MIL for reducing O_2 into $^{\bullet}O_2^-$. Nevertheless, the DMPO-$^{\bullet}O_2^-$ peaks for Cu-NPEB and Cu-SAEB are dramatically enhanced compared to those of MIL (Figure 2e,f). This is because the photo-generated electrons with higher reduction potential (originating from MIL) can be retained for reducing O_2 to $^{\bullet}O_2^-$ in these two Z-scheme photocatalysts. These phenomena demonstrate that conventional type-II charge transport is improbable for Cu-NPEB and Cu-SAEB. Instead, Z-scheme charge transfer is more likely to occur (Figure 2h,i). In comparison, Cu-SAEB has

much stronger DMPO-$^{\bullet}O_2^-$ peaks than those of Cu-NPEB, indicating that N–Cu_1–S species can transport charges much more efficiently than that of Cu NPs at the Z-scheme contact interface. N–Cu_1–S species serve as SAEBs to achieve efficient Z-scheme interfacial charge transfer in Cu-SAEB. As a result, the accumulation of photo-generated carriers with strong redox potential can be greatly improved under light irradiation.

Due to the Z-scheme charge-transfer characteristics in Cu-SAEB, we evaluated its photocatalytic CO_2RR performance under simulated solar irradiation without any sacrificial reagents or photosensitizers in pure water (details are shown in the Supporting Information). To investigate the optimized amounts of Cu content in Cu_1/MS and the optimized mass ratio between Cu_1/MS and MIL in the encapsulation structure, a series of samples have been synthesized. As shown in Figures S24–S26, the Cu content of Cu_1/MS and the mass ratio between Cu_1/MS and MIL have a significant influence on the photocatalytic CO_2RR performances over these encapsulation structures. Figure 3a,b shows that the photocatalytic CO evolution rate of Cu-SAEB is about

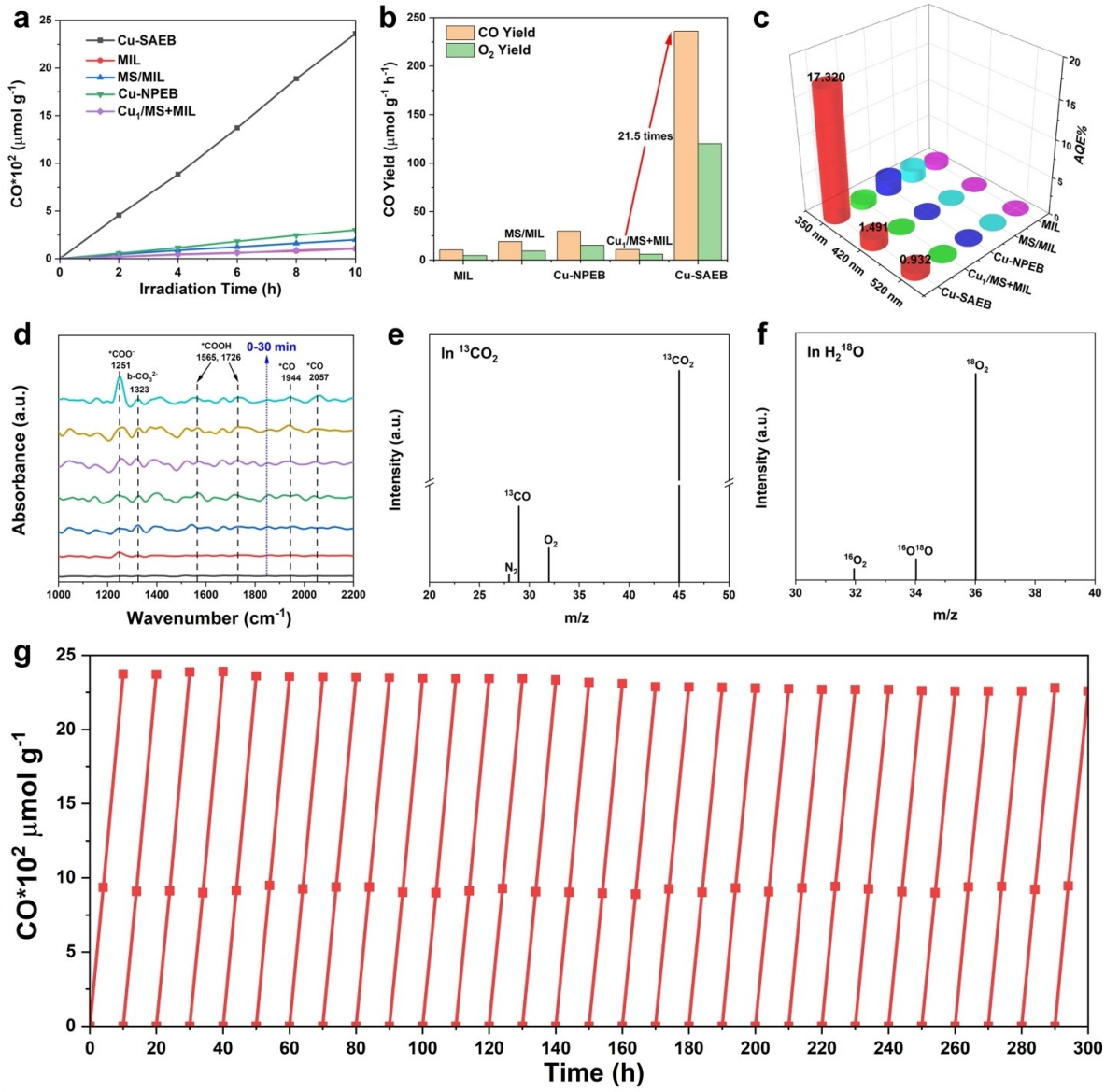

Figure 3. (a) Time-dependent photocatalytic CO_2 reduction to CO over samples. (b) Evolution rates of CO and O_2 over samples. (c) AQE% of samples under light irradiation with 350, 420, and 520 nm wavelength, respectively. (d) In situ FTIR experiment over Cu-SAEB under light irradiation. (e) $^{13}CO_2$ and (f) $H_2{}^{18}O$ labeling experiments over Cu-SAEB. (g) The repeated cycles of photocatalytic CO_2RR over Cu-SAEB.

236.0 μmol g^{-1} h^{-1}, and this value is one of the best reported for CO_2 photoreduction (Table S3). It is about 21.5 times better compared with that of Cu_1/MS + MIL. The Cu-NPEB and MS/MIL display CO evolution rates of 29.8 and 19.1 μmol g^{-1} h^{-1} respectively, which are also much lower than that of Cu-SAEB. These values imply that the unique encapsulation structure and the existence of N–Cu_1–S SAEBs contribute to the enhancement of photocatalytic CO_2RR performance over Cu-SAEBs. Moreover, due to the absence of sacrificial reagents, the molar ratio of CO and O_2 evolution rates (Figure 3b) is close to two. Only small amounts of CH_4 (selectivity < 1%) can be formed.

The apparent quantum efficiencies (AQE%) of Cu-SAEBs are about 17.320, 1.491, and 0.932% at 350, 420, and 520 nm, respectively (Figure 3c and Figure S27), which are much higher than those for references (details are shown in the Supporting Information). Control experiments were also conducted; i.e., in the absence of light, CO_2, and catalyst (Figure S28). No CO product can be detected, implying that light irradiation, CO_2, and photocatalyst are conditions required for photocatalytic CO_2RR over Cu-SAEB. The photocatalytic CO_2 reduction of MS and Cu_1/MS was also performed for comparison (Figure S29).

In situ Fourier-transform infrared (in situ FTIR) spectroscopy was performed to correlate surface characteristics to the efficiency of photocatalytic CO_2RR. As shown in Figure 3d, the gradually increasing bands at 1251 cm^{-1} can be assigned to the vibrations of *COO^-, which is favorable for the formation of a *COOH intermediate.[9a] A band at 1323 cm^{-1} corresponds to bidentate carbonate (b-CO_3^{2-})

groups due to chemisorbed CO_2 on the photocatalyst.[9b] A new band at around 1565 cm^{-1} is ascribed to *COOH groups, which are regarded as one of the most crucial intermediates for converting CO_2 to CO.[9c] The band at about 1726 cm^{-1} represents C=O stretching vibrations in *COOH.[9d] Bands at about 1944 and 2057 cm^{-1} are assigned to the *CO intermediate.[9e,f] Based on these results, a plausible mechanism of CO_2RR over Cu-SAEB is proposed: 1: $CO_2(g) \rightarrow *CO_2$; 2: $*CO_2 + e^- \rightarrow *COO^-$; 3: $*COO^- + H^+ \rightarrow *COOH$; 4: $*COOH + H^+ + e^- \rightarrow *CO + H_2O$; 5: $*CO \rightarrow CO(g)$, where the asterisk (*) represents the adsorption state on the photocatalyst surface. To further confirm the conversion of CO_2 and H_2O to CO and O_2, $^{13}CO_2$ and $H_2{}^{18}O$ isotope labeling and control experiments were conducted (Figure 3e,f and Figure S30). The peaks at $m/z = 29$ (^{13}CO) and $m/z = 36$ ($^{18}O_2$) prove that the formation of CO and O_2 can be derived from CO_2 and H_2O, respectively. Cycling measurements were carried out to evaluate the stability of the photocatalytic CO_2RR. As shown in Figure 3g, Cu-SAEB exhibits exceptional long-term stability under the photocatalytic processes. No obvious deactivation can be observed over 30 cycles of 300 h. The phase composition and morphology of the used Cu-SAEB also did not change, demonstrating its favorable photocatalytic stability (Figures S31–S34).

We studied charge-carrier dynamics to investigate the cause of the enhanced photocatalytic activity of Cu-SAEB. Photoelectron generation and transfer were evaluated with a single-particle photoluminescence (PL) microscope equipped with a picosecond laser and an electron multiplying charge-coupled device camera. As shown in Figure 4a–d, all samples exhibit bright areas with circular shapes. MIL displays the brightest single-particle PL image among the samples (Figure 4a). This means that the recombination rate of photo-generated carriers is the highest in MIL among these samples, which is detrimental to photocatalytic efficiency. The brightness of the single-particle PL images is lower for MS/MIL and Cu-NPEB (Figure 4b,c), implying lower recombination of charge carriers. As shown in Figure 4d, the lowest brightness can be observed for Cu-SAEB.

The dramatic PL quenching in Cu-SAEB suggests that charge carriers rapidly separate and migrate during light irradiation. Furthermore, their separation efficiency was

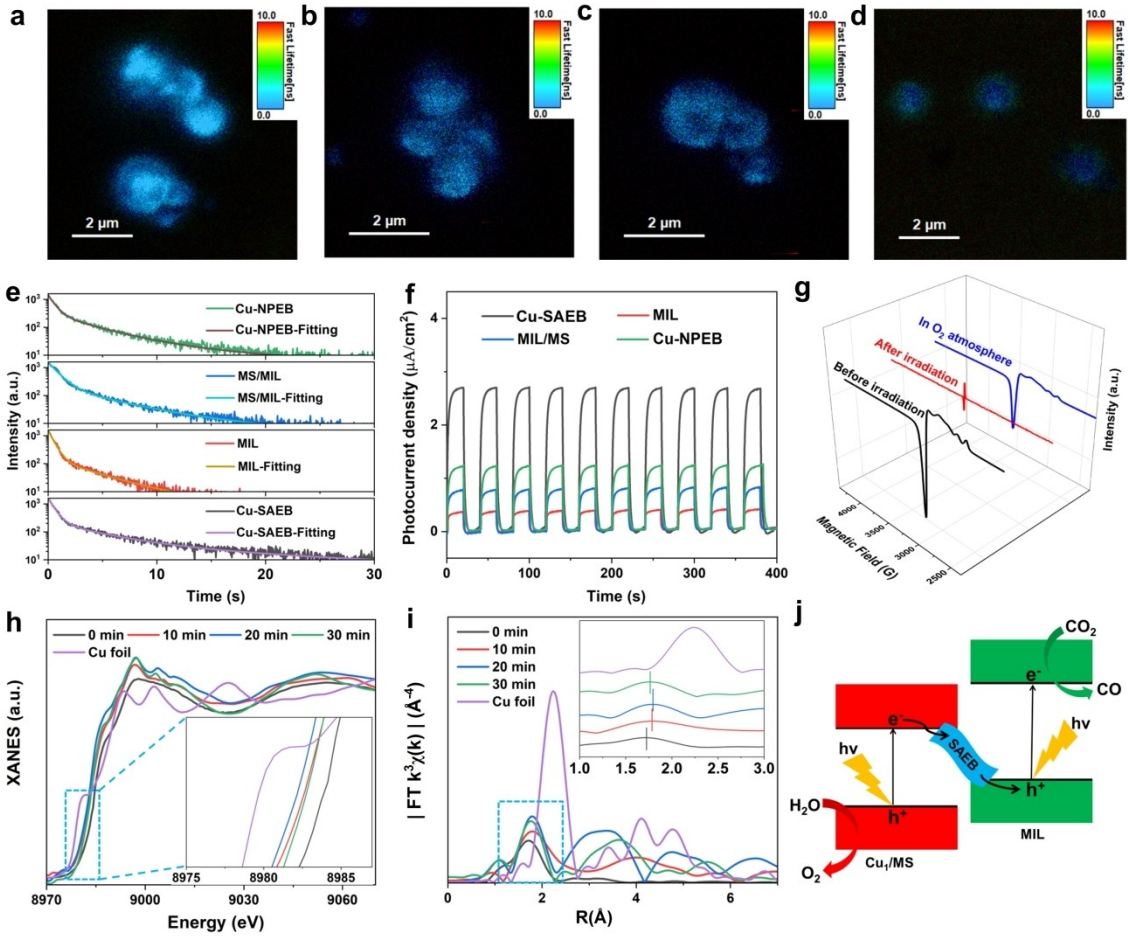

Figure 4. Single-particle PL images of (a) MIL, (b) MS/MIL, (c) Cu-NPEB, and (d) Cu-SAEB. (e) Time-resolved transient PL decay. (f) Transient photocurrent spectra. (g) In situ EPR measurement of Cu-SAEB. (h) Quasi in situ XANES and (i) FT-EXAFS spectra of Cu K-edge over Cu-SAEB after 0, 10, 20, 30 min light irradiation under Ar atmosphere, without CO_2 and water. (j) Illustration of the charge-transfer pathway under light irradiation over Cu-SAEB.

also quantified by calculating the average PL lifetimes. Cu-SAEB possesses the longest lifetime (7.72 ns) among the samples (Figure 4e and Table S4), which is in accordance with the steady-state PL spectra (Figure S35). Charge-transfer properties can also be studied via transient photocurrent response and electrochemical impedance spectroscopy (EIS) measurements. Cu-SAEB displays significantly enhanced photocurrent density (Figure 4f) and lower charge-transfer resistance (Figure S36) compared with those of other samples, implying that more effective charge separation and transmission have been achieved in Cu-SAEB. Based on these results, we can confirm that the SAEB of N–Cu_1–S greatly enhances the separation and transmission efficiency of charge carriers. This results in higher photocatalytic CO_2RR activity for Cu-SAEB.

To gain direct experimental evidence for the N–Cu_1–S coordination structures acting as EBs, we conducted in situ low-temperature X-band electron paramagnetic resonance (EPR) (Figure 4g and Figure S37). The characteristic signal of Cu^{2+} disappeared due to the reduction of Cu^{2+} to EPR-silent Cu^{1+} after light irradiation in the methanol solution (Figure S37). The characteristic signal of Ti^{3+} appears after light irradiation (Figure S37), indicating the possible reduction sites on Ti species during the photocatalytic reaction. After exposing Cu-SAEB to oxygen atmosphere, we obtained the same EPR spectrum as before irradiation. This indicates that the EPR-silent Cu^{1+} can be easily oxidized to the "before irradiation" state. In addition, quasi in situ XAFS characterization was employed to find more definitive evidence for the charge-transfer behavior of SAEB in Cu-SAEB. The Cu K-edge XANES spectra of Cu-SAEB was collected at different irradiation times. As shown in Figure 4h, an obviously negative shift of the Cu K-edge near-edge spectra can be observed in the 10th and 20th minutes, indicating the partial reduction of Cu, which corresponds with the in situ EPR results. As for the spectrum obtained at 30 min (Figure 4h), the near-edge Cu K-edge spectrum displays a positive shift compared to that obtained at 20 min, which suggests that the Cu in the SAEB tends to be oxidized to the initial state as the irradiation time is prolonged. In other words, the Cu in the SAEB can be partially reduced after capturing the photo-generated electrons at the beginning of the light irradiation. Then, the photo-generated holes (retained in the ligand of MIL) can transfer via the SAEB of the N–Cu_1–S structure to oxidize the reduced Cu species to the initial state. These results are further verified by the FT-EXAFS spectrum (Figure 4i), in which the main backscattering peak of Cu in Cu-SAEB gradually shifted to the larger radial distance, and then shifted back towards the initial state during light irradiation. Therefore, the quasi in situ XAFS results provide strong evidence to prove the SAEB role of N–Cu_1–S during photocatalytic processes. Based on the above results, we propose a possible charge-transfer pathway in Cu-SAEB under light irradiation (Figure 4j). Both Cu_1/MS and MIL can be excited to generate electrons and holes under light irradiation in Cu-SAEB. The photo-generated electrons originating from Cu_1/MS and MIL are captured by Cu and Ti species, respectively, according to the in situ EPR and quasi in situ XAFS results. Meanwhile, photo-generated holes originating from MIL can be trapped by the organic ligand due to the ligand-to-metal-cluster charge-transfer (LCCT) mechanism. These processes enable efficient Z-scheme recombination of the electrons on Cu species and holes trapped at the organic ligands of MIL, due to the formation of N–Cu_1–S SAEBs at the Cu-SAEB contact interface. Eventually, the photo-generated carriers with stronger redox potential efficiently separate and reduce CO_2 to CO while oxidizing H_2O to O_2 over Cu-SAEB.

DFT calculations were employed to investigate the electronic structure of Cu-SAEB and the charge-transfer mechanism. By combining experimental data and theoretical simulations, we have confirmed that the N–Cu_1–S structure is the most favorable configuration at the interface of Cu-SAEB (Figures S16 and S38). The density of states (DOS) calculations show a narrower band gap for Cu_1/MS compared with that of MS (Figure S39), which is consistent with the experimental results (Figure 2a). Figure 5a exhibits the presence of partial DOS of Cu near both CBM and VBM (valence band maximum) after the formation of Cu-SAEB. Moreover, the charge-density difference of Cu-SAEB exhibits that N–Cu_1–S is surrounded by both electron depletion and accumulation areas (Figure 5b,c). This reinforces that the N–Cu_1–S species can act as an SAEB for achieving the Z-scheme charge-transfer mode in Cu-SAEB. The charge-transfer pathway was further investigated at the contact interface of Cu-SAEB under light irradiation by introducing an extra electron to act as a simulated photo-generated

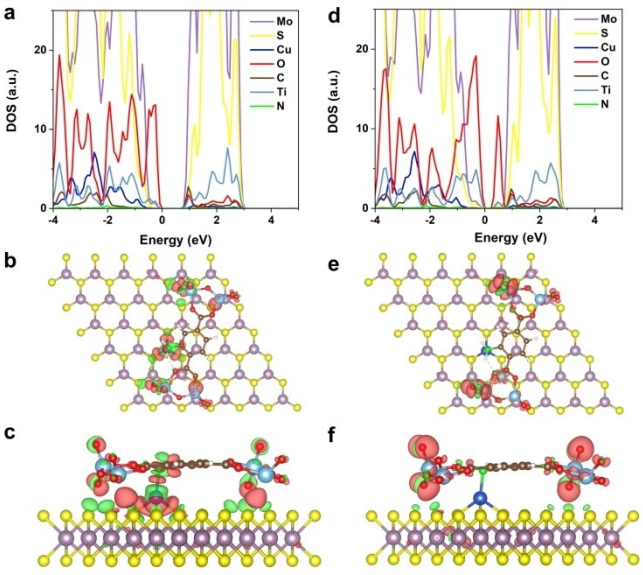

Figure 5. (a) The DOS of Cu-SAEB before photo-excitation. The charge-density difference of Cu-SAEB before photo-excitation (b) top view, and (c) side view. (d) The DOS of Cu-SAEB after photo-excitation. The charge-density difference between before and after photo-excitation over Cu-SAEB (e) top view and (f) side view. Red and green iso-surfaces represent electron accumulation and depletion, respectively, and the iso-surface levels are set to 0.004 e Å^{-3} for (b),(c) and 0.0006 e Å^{-3} for (e),(f). Atom key: Cu (blue), N (green), S (yellow), C (brown), Ti (cyan), O (red), Mo (pink), and H (white).

electron. After the relaxation of the simulated "photogenerated electron" (Figure 5d–f), it tended to distribute around the Ti–O clusters in Cu-SAEB. These phenomena suggest that Ti–O clusters serve as electron traps during light irradiation, which can further function as active sites for the reduction of CO_2. Moreover, by comparing the charge-density difference between Cu NPs/MS and Cu_1/MS, we find that N–Cu_1–S SAEB has a much more efficient charge-transfer ability than that of Cu NPs at the interface (Figure S40). These observations explain the excellent photocatalytic activity of Cu-SAEB well.

Conclusion

In summary, we have presented Cu-SAEB Z-scheme photocatalysts containing single-atom N–Cu_1–S electron bridges at its contact interface. Notably, Cu-SAEB displays superior activity and long-term stability for the photocatalytic CO_2 reduction reaction without using any sacrificial agents. The dynamics of charge carriers and mechanistic investigations confirm that N–Cu_1–S serves as a SAEB to achieve an efficient Z-scheme charge-transfer mode at the contact interface of Cu-SAEB, and thereby it maintains photogenerated carriers with a strong redox potential to ultimately enhance the photocatalytic CO_2 performance. This study presents a new direction for designing highly active photocatalysts with atomic precision and it demonstrates the power of interfacial structures in photocatalytic processes.

Acknowledgements

This work was supported by the National Natural Science Foundation of China (21971002, 22202011), the Natural Science Research Project of Higher education in Anhui Province (2022AH020020), and Natural Science Foundation of Shandong Province (ZR2022QB056). The authors thank the BL14W1 station in the Shanghai Synchrotron Radiation Facility (SSRF) and the 1W1B station in the Beijing Synchrotron Radiation Facility (BSRF) for help with characterization.

Conflict of Interest

The authors declare no conflict of interest.

Data Availability Statement

The data that support the findings of this study are available from the corresponding author upon reasonable request.

Keywords: CO_2RR · Electron Bridge · MIL-125-NH_2 · Single-Atom · Z-Scheme

[1] a) J. Gong, C. Li, M. R. Wasielewski, *Chem. Soc. Rev.* **2019**, *48*, 1862–1864; b) T. Kong, Y. Jiang, Y. Xiong, *Chem. Soc. Rev.* **2020**, *49*, 6579–6591.

[2] a) J. Bian, Z. Zhang, J. Feng, M. Thangamuthu, F. Yang, L. Sun, Z. Li, Y. Qu, D. Tang, Z. Lin, F. Bai, J. Tang, L. Jing, *Angew. Chem. Int. Ed.* **2021**, *60*, 20906–20914; *Angew. Chem.* **2021**, *133*, 21074–21082; b) Y. Wang, Z. Zhang, L. Zhang, Z. Luo, J. Shen, H. Lin, J. Long, J. C. S. Wu, X. Fu, X. Wang, C. Li, *J. Am. Chem. Soc.* **2018**, *140*, 14595–14598.

[3] a) D. Zhao, C. Dong, B. Wang, C. Chen, Y. Huang, Z. Diao, S. Li, L. Guo, S. Shen, *Adv. Mater.* **2019**, *31*, 1903545; b) B. Ma, G. Chen, C. Fave, L. Chen, R. Kuriki, K. Maeda, O. Ishitani, T.-C. Lau, J. Bonin, M. Robert, *J. Am. Chem. Soc.* **2020**, *142*, 6188–6195; c) W. Jiang, J. Low, K. Mao, D. Duan, S. Chen, W. Liu, C.-W. Pao, J. Ma, S. Sang, C. Shu, X. Zhan, Z. Qi, H. Zhang, Z. Liu, X. Wu, R. Long, L. Song, Y. Xiong, *J. Am. Chem. Soc.* **2021**, *143*, 269–278; d) W. Zhang, A. R. Mohamed, W.-J. Ong, *Angew. Chem. Int. Ed.* **2020**, *59*, 22894–22915; *Angew. Chem.* **2020**, *132*, 23092–23115; e) Z. Xin, Y. Gao, Y. Gao, H. Song, J. Zhao, F. Fan, A. Xia, X. Li, C.-H. Tung, L. Wu, *Adv. Mater.* **2022**, *34*, 2106662.

[4] a) T. Oshima, S. Nishioka, Y. Kikuchi, S. Hirai, K.-i. Yanagisawa, M. Eguchi, Y. Miseki, T. Yokoi, T. Yui, K. Kimoto, K. Sayama, O. Ishitani, T. E. Mallouk, K. Maeda, *J. Am. Chem. Soc.* **2020**, *142*, 8412–8420; b) S. Yoshino, A. Iwase, Y. Yamaguchi, T. M. Suzuki, T. Morikawa, A. Kudo, *J. Am. Chem. Soc.* **2022**, *144*, 2323–2332; c) K. Zheng, Y. Wu, J. Zhu, M. Wu, X. Jiao, L. Li, S. Wang, M. Fan, J. Hu, W. Yan, J. Zhu, Y. Sun, Y. Xie, *J. Am. Chem. Soc.* **2022**, *144*, 12357–12366; d) S. Chen, J. J. M. Vequizo, Z. Pan, T. Hisatomi, M. Nakabayashi, L. Lin, Z. Wang, K. Kato, A. Yamakata, N. Shibata, T. Takata, T. Yamada, K. Domen, *J. Am. Chem. Soc.* **2021**, *143*, 10633–10641.

[5] a) S. Yoshino, T. Takayama, Y. Yamaguchi, A. Iwase, A. Kudo, *Acc. Chem. Res.* **2022**, *55*, 966–977; b) J. Jing, J. Yang, W. Li, Z. Wu, Y. Zhu, *Adv. Mater.* **2022**, *34*, 2106807.

[6] a) W. Zhong, R. Sa, L. Li, Y. He, L. Li, J. Bi, Z. Zhuang, Y. Yu, Z. Zou, *J. Am. Chem. Soc.* **2019**, *141*, 7615–7621; b) G. Wang, Y. Liu, N. Zhao, H. Chen, W. Wu, Y. Li, X. Liu, A. Li, W. Chen, J. Mao, *Nano Res.* **2022**, *15*, 7034–7041; c) S. Cao, H. Li, T. Tong, H.-C. Chen, A. Yu, J. Yu, H. Chen, *Adv. Funct. Mater.* **2018**, *28*, 1802169; d) Z. Zhuang, L. Xia, J. Huang, P. Zhu, Y. Li, C. Ye, M. Xia, R. Yu, Z. Lang, J. Zhu, L. Zheng, Y. Wang, T. Zhai, Y. Zhao, S. Wei, L. Li, D. Wang, Y. Li, *Angew. Chem. Int. Ed.* **2023**, *62*, e202212335; *Angew. Chem.* **2023**, *135*, e202212335; e) L. Zhou, J. M. P. Martirez, J. Finzel, C. Zhang, D. F. Swearer, S. Tian, H. Robatjazi, M. Lou, L. Dong, L. Henderson, P. Christopher, E. A. Carter, P. Nordlander, N. J. Halas, *Nat. Energy* **2020**, *5*, 61–70; f) J. Li, H. Huang, W. Xue, K. Sun, X. Song, C. Wu, L. Nie, Y. Li, C. Liu, Y. Pan, H. Jiang, D. Mei, C. Zhong, *Nat. Catal.* **2021**, *4*, 719–729; g) C. Wang, K. Wang, Y. Feng, C. Li, X. Zhou, L. Gan, Y. Feng, H. Zhou, B. Zhang, X. Qu, H. Li, J. Li, A. Li, Y. Sun, S. Zhang, G. Yang, Y. Guo, S. Yang, T. Zhou, F. Dong, K. Zheng, L. Wang, J. Huang, Z. Zhang, X. Han, *Adv. Mater.* **2021**, *33*, 2003327; h) W. Wang, H. Zhang, S. Zhang, Y. Liu, G. Wang, C. Sun, H. Zhao, *Angew. Chem. Int. Ed.* **2019**, *58*, 16644–16650; *Angew. Chem.* **2019**, *131*, 16797–16803; i) W. H. Li, J. Yang, D. Wang, *Angew. Chem. Int. Ed.* **2022**, *61*, e202213318; *Angew. Chem.* **2022**, *134*, e202213318; j) Z. Zhang, J. Zhu, S. Chen, W. Sun, D. Wang, *Angew. Chem. Int. Ed.* **2023**, *62*, e202215136; *Angew. Chem.* **2023**, *135*, e202215136.

[7] a) Y. Zhang, B. Xia, J. Ran, K. Davey, S. Qiao, *Adv. Energy Mater.* **2020**, *10*, 1903879; b) S. Ji, Y. Qu, T. Wang, Y. Chen, G. Wang, X. Li, J. Dong, Q. Chen, W. Zhang, Z. Zhang, S. Liang, R. Yu, Y. Wang, D. Wang, Y. Li, *Angew. Chem. Int. Ed.* **2020**, *59*, 10651–10657; *Angew. Chem.* **2020**, *132*, 10738–10744; c) Z.

Teng, Q. Zhang, H. Yang, K. Kato, W. Yang, Y. Lu, S. Liu, C. Wang, A. Yamakata, C. Su, B. Liu, T. Ohno, *Nat. Catal.* **2021**, *4*, 374–384; d) G. Wang, C. He, R. Huang, J. Mao, D. Wang, Y. Li, *J. Am. Chem. Soc.* **2020**, *142*, 19339–19345; e) P. Zhu, X. Xiong, D. S. Wang, *Nano Res.* **2022**, *15*, 5792–5815; f) G. Wang, R. Huang, J. Zhang, J. Mao, D. Wang, Y. Li, *Adv. Mater.* **2021**, *33*, 2105904.

[8] a) C. Chu, Q. Zhu, Z. Pan, S. Gupta, D. Huang, Y. Du, S. Weon, Y. Wu, C. Muhich, E. Stavitski, K. Domen, J.-H. Kim, *Proc. Natl. Acad. Sci. USA* **2020**, *117*, 6376–6382; b) S. Hejazi, S. Mohajernia, B. Osuagwu, G. Zoppellaro, P. Andryskova, O. Tomanec, S. Kment, R. Zbořil, P. Schmuki, *Adv. Mater.* **2020**, *32*, 1908505; c) X. Jin, R. Wang, L. Zhang, R. Si, M. Shen, M. Wang, J. Tian, J. Shi, *Angew. Chem. Int. Ed.* **2020**, *59*, 6827–6831; *Angew. Chem.* **2020**, *132*, 6894–6898; d) Q. Li, S. Wang, Z. Sun, Q. Tang, Y. Liu, L. Wang, H. Wang, Z. Wu, *Nano Res.* **2019**, *12*, 2749–2759; e) R. Z. Li, D. S. Wang, *Nano Res.* **2022**, *15*, 6888–6923; f) G. Wang, Z. Chen, T. Wang, D. Wang, J. Mao, *Angew. Chem. Int. Ed.* **2022**, *61*, e202210789; *Angew. Chem.* **2022**, *134*, e202210789.

[9] a) X. Chen, C. Peng, W. Dan, L. Yu, Y. Wu, H. Fei, *Nat. Commun.* **2022**, *13*, 4592; b) M. Lusardi, T. Struble, A. R. Teixeira, K. F. Jensen, *Catal. Sci. Technol.* **2020**, *10*, 536–548; c) X. Zu, Y. Zhao, X. Li, R. Chen, W. Shao, Z. Wang, J. Hu, J. Zhu, Y. Pan, Y. Sun, Y. Xie, *Angew. Chem. Int. Ed.* **2021**, *60*, 13840–13846; *Angew. Chem.* **2021**, *133*, 13959–13965; d) R. H. Ellerbrock, H. H. Gerke, *J. Plant Nutr. Soil Sci.* **2021**, *184*, 388–397; e) D. Zeng, X. Wang, Y. Liu, D. Liu, Z. Zhang, L. Fei, J. Robertson, C. Kuai, Y. Guo, *ACS Sustainable Chem. Eng.* **2022**, *10*, 5758–5769; f) X. Li, Y. Sun, J. Xu, Y. Shao, J. Wu, X. Xu, Y. Pan, H. Ju, J. Zhu, Y. Xie, *Nat. Energy* **2019**, *4*, 690–699.

Manuscript received: December 14, 2022
Accepted manuscript online: February 7, 2023
Version of record online: February 20, 2023